

# Supplementary materials for “Correlation between electronic configuration and magnetic stability in dysprosium single atom magnets”

*Fabio Donati<sup>1,2,\*</sup>, Marina Pivetta<sup>3</sup>, Christoph Wolf<sup>1,4</sup>, Aparajita Singha<sup>1,4,5</sup>, Christian Wäckerlin<sup>3,6</sup>, Romana Baltic<sup>3</sup>, Edgar Fernandes<sup>3</sup>, Jean-Guillaume de Groot<sup>3</sup>, Safa Lamia Ahmed<sup>1,2</sup>, Luca Persichetti<sup>7,8</sup>, Corneliu Nistor<sup>7</sup>, Jan Dreiser<sup>9</sup>, Alessandro Barla<sup>10</sup>, Pietro Gambardella<sup>7</sup>, Harald Brune<sup>3</sup>, and Stefano Rusponi<sup>3,\*</sup>*

<sup>1</sup>Center for Quantum Nanoscience, Institute for Basic Science (IBS), Seoul 03760, Republic of Korea

<sup>2</sup>Department of Physics, Ewha Womans University, Seoul 03760, Republic of Korea

<sup>3</sup>Institute of Physics, École Polytechnique Fédérale de Lausanne, Station 3, CH-1015 Lausanne, Switzerland

<sup>4</sup>Ewha Womans University, Seoul 03760, Republic of Korea

<sup>5</sup>Max Planck Institute for Solid State Research, Stuttgart, Germany

<sup>6</sup>Surface Science and Coating Technologies, Empa - Swiss Federal Laboratories for Materials Research and Technology, Überlandstrasse 129, 8600 Dübendorf, Switzerland

<sup>7</sup>Department of Materials, ETH Zurich, Hönggerberggring 64, CH-8093 Zurich, Switzerland

<sup>8</sup>Department of Sciences, Roma Tre University, I-00146, Roma, Italy

<sup>9</sup>Swiss Light Source (SLS), Paul Scherrer Institute (PSI), CH-5232 Villigen PSI, Switzerland

<sup>10</sup>Istituto di Struttura della Materia (ISM), Consiglio Nazionale delle Ricerche (CNR), I-34149  
Trieste, Italy

## Corresponding Authors

\*donati.fabio@qns.science, stefano.rusponi@epfl.ch

## 1. Experimental details

### A. Sample preparation.

Single crystals of Ag(100) were prepared by repeated cycles of sputtering and subsequent annealing to 773 K. For the XAS/XMCD experiments, MgO films with thickness between 2.5 and 9.0 monolayers (MLs) were grown by thermal evaporation of Mg in O<sub>2</sub> partial pressure of  $1 \times 10^{-6}$  mbar, with the substrate kept at 623 K and a Mg flux yielding a growth rate of about 0.2 ML/min. One monolayer is defined as one MgO(100) unit cell per Ag(100) substrate atom. The calibration of the MgO thickness was performed by measuring the Mg XAS K edge and comparing it to previous results.<sup>1</sup> The MgO/Ag(100) samples were transferred to the measurement position without breaking the vacuum. Dysprosium atoms were deposited from thoroughly degassed rods (purity 99 %), directly onto the substrate held at less than 10 K and in a base pressure of  $2 \times 10^{-11}$  mbar. Also for Dy, we define 1 ML as one lanthanide atom per Ag(100) substrate atom, and calibrate the amount by comparison with former experiments.<sup>1</sup>

For the STM experiments, MgO films with nominal thickness between 1 and 3 MLs were grown by thermal evaporation of Mg in O<sub>2</sub> partial pressure of  $1 \times 10^{-6}$  mbar, with the substrate kept at 750 K. Different MgO thicknesses coexist on the same sample and are identified by differential conductance spectroscopy.<sup>2, 3</sup> Dysprosium atoms were deposited from thoroughly degassed rods (purity 99 %), directly onto the substrate held at 10 K and in a base pressure of  $1 \times 10^{-10}$  mbar. The Dy coverage is determined by counting the number of adatoms in a given surface area.

#### *B. XAS/XMCD measurements.*

The XAS and XMCD measurements were performed at the EPFL/PSI X-Treme beamline at the Swiss Light Source.<sup>4</sup> The endstation is equipped with an ultra-high vacuum chamber for sample preparation (base pressure  $5 \times 10^{-10}$  mbar) and an Omicron variable-temperature scanning tunneling microscope (VT-STM). All measurements were performed with circularly polarized light in the total electron yield mode at sample temperatures of  $T = 2.5$  K, and in external magnetic fields up to  $B = 6.8$  T parallel to the x-ray beam. In order to isolate the contribution of the Dy atoms from the background signal, spectra of bare MgO/Ag(100) over the Dy M<sub>4,5</sub> edge are recorded for each sample prior to Dy deposition and subtracted from the final spectra. Hysteresis loops and magnetic relaxations were obtained by acquiring the XAS signal for the two circular polarizations at the XMCD peak corresponding to the 4f occupation of interest, 1290.5 eV for 4f<sup>9</sup> and 1288.3 eV for 4f<sup>10</sup>, respectively. For the hysteresis loops, the field-evolution of the two polarizations has been acquired separately in two subsequent loops. For the magnetic relaxation, XAS signal at alternating polarization was acquired as a function of time after saturating the ensemble to  $B = +3$  T. During the sweep of the magnetic field from the saturating to the measurement value, the beam shutter was kept closed to prevent undesired photon-induced relaxation. In this way, the ensemble is largely preserved in its saturated state until the beginning of the measurement. For both hysteresis

and relaxation measurements, the XAS from the two opposite polarizations was normalized to the corresponding pre-edge signal measured at 1281.3 eV, also acquired in the same sequence, to compensate for any spurious variation of the beam intensity during the acquisition. In order to minimize the influence of the photon beam on the lifetime of the magnetic atoms,<sup>5</sup> all the measurements were performed at the smallest photon flux ensuring a sufficient signal to noise ratio. For spectra and hysteresis loops, we used  $\phi = 0.55 \times 10^{-2} \text{ nm}^{-2} \text{ s}^{-1}$ , while for relaxation curves  $\phi = 0.14 \times 10^{-2} \text{ nm}^{-2} \text{ s}^{-1}$ .<sup>1, 5</sup>

### *C. STM measurements.*

STM measurements were performed with a home-built STM at 5 K using W tips. The STM images were acquired in constant-current mode with the tunnel voltage applied to the sample.

## **2. Identification of the adsorption sites of Dy atoms**

We determine the adsorption site of the Dy species by co-evaporating Dy and Co, as the latter, adsorbing on O-top site, acts as a marker for O lattice positions.<sup>1-3</sup> Figure S1 shows a 2 ML MgO region with co-evaporated Dy and Co. The overlaid MgO lattice, with white (black) dots representing oxygen (magnesium) atoms, is extracted from atomically resolved images of the MgO substrate. By aligning the white dots (O atoms) with the Co adatoms, one observes that the Dy adatoms with lower apparent height are adsorbed on O-top sites, while the species with higher apparent height adsorb on bridge sites. Hence, we identify the former as Dy<sup>top</sup> and the latter as Dy<sup>br</sup>.

The change in abundance of  $\text{Dy}^{\text{top}}$  and  $\text{Dy}^{\text{br}}$  species between the first and second layer has been previously observed for Ho,<sup>1,2</sup> Tb, and Er.<sup>3</sup> The neat change in the favored adsorption site is mostly due to the MgO thickness dependent energy associated with the bonding formation and structural distortion resulting in a modified position of the MgO surface atoms. The adsorption on the bridge site allows the formation of a double bond with the surface oxygen which lowers the energy of the system. However, such a bonding configuration requires a more pronounced structural distortion of the MgO surface, which becomes less favorable as the thickness of the MgO film increases due to the increase of the stiffness of the MgO structure. Therefore, adsorption on bridge site becomes less favorable already starting from 2 ML MgO.<sup>2,3</sup>

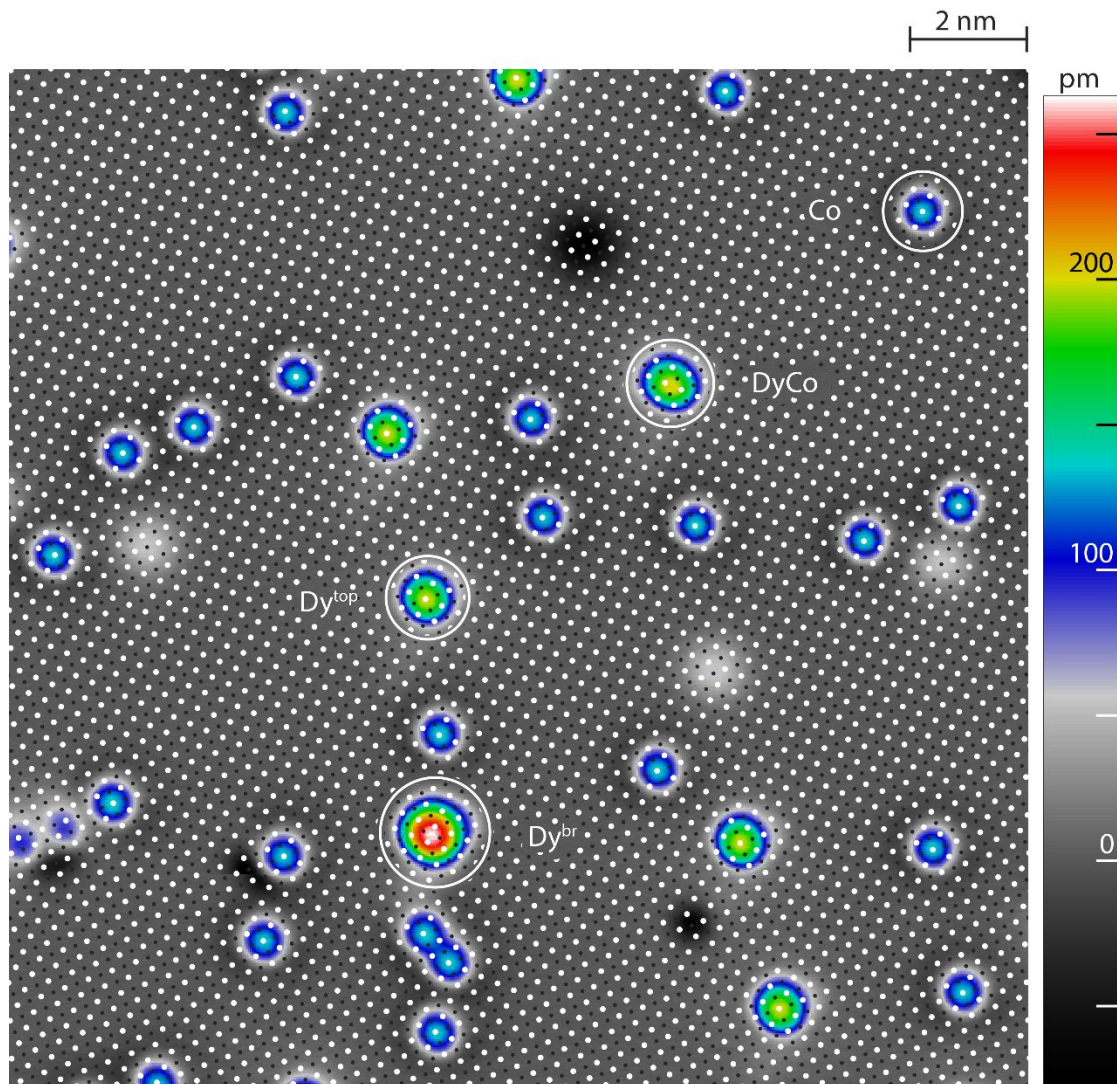


**Figure S1.** Identification of the adsorption site of Dy atoms. STM image of co-deposited Dy and Co on 2 ML MgO/Ag(100). The MgO lattice is extracted from atomically resolved images of the substrate. The white dots, representing the O atoms of the MgO lattice, are brought into coincidence with the Co adatoms. The black dots correspond to the position of Mg atoms. An elongated object is identified as a DyCo heterodimer. ( $V_t = -100$  mV,  $I_t = 20$  pA,  $T_{STM} = 5$  K).

### 3. Details of multiplet calculations

XAS and XMCD spectra of the individual species have been calculated using the MultiX code.<sup>6</sup> The electron-electron interaction has been rescaled by 0.80 and 0.75 for Dy  $4f^9$  and  $4f^{10}$ , respectively, to match the spectral shape observed in experiments. A core-hole broadening of 0.6 eV gave best match with the data linewidth. For the different species, we simulated spectra using a point charges model. The position and intensity of the nearest neighbors' charges have been obtained from DFT, with the intensity provided in terms of Born effective charges. For the Dy  $4f^9$  species, we used the coordinates obtained for Dy on MgO/Ag(100), while for Dy  $4f^{10}$  species we adopted the structure calculated for the Dy atoms on bare MgO (see Sec. S6). The position and intensity of the point charges are reported in Tables 1-4.

As mentioned in the text, the use of Born effective charges gives a level splitting for  $4f^9$  Dy<sup>top</sup> that overestimates previous values of spin-switching thresholds from STM experiments,<sup>7</sup> with a 0.8 rescaling factor on the intensities required to match the reported values. Due to the large energy splitting, this rescaling does not affect the shape of the XAS and XMCD spectra, which mostly reflects the population of the lowest states. On the other hand, the Löwdin analysis gives charge intensities about 50% smaller than the Born values, leading to large underestimation of the level splitting. Although the optimal charge values seem to lie in between the two analyses, the Born charges provide a better approximation to the effective crystal field generated by the Mg and O ions.

**Table S1.** Point charge crystal field for  $4f^9$  Dy<sup>top</sup> atoms. Coordinates (X,Y,Z) are provided in Å, while the charge intensity Q is given in multiples of electron charge.

Element	X	Y	Z	Q
O	0.000	0.000	-2.012	-2
O	-2.072	-2.072	-2.732	-2
O	-2.072	2.072	-2.732	-2
O	2.072	2.072	-2.732	-2
O	2.072	-2.072	-2.732	-2
Mg	-2.143	0.000	-2.771	2
Mg	0.000	2.143	-2.771	2
Mg	2.143	0.000	-2.771	2
Mg	0.000	-2.143	-2.771	2

**Table S2.** Point charge crystal field for  $4f^9$  Dy<sup>br</sup> atoms. Coordinates (X,Y,Z) are provided in Å, while the charge intensity Q is given in multiples of electron charge.

Element	X	Y	Z	Q
O	-0.994	-0.994	-1.739	-2
O	0.994	0.994	-1.739	-2
Mg	-1.114	1.114	-2.451	2
Mg	1.114	-1.114	-2.451	2



**Table S3.** Point charge crystal field for  $4f^{10}$  Dy<sup>top</sup> atoms. Coordinates (X,Y,Z) are provided in Å, while the charge intensity Q is given in multiples of electron charge.

Element	X	Y	Z	Q
O	0.000	0.000	-2.204	-2
O	-2.077	-2.077	-2.714	-2
O	-2.077	2.077	-2.714	-2
O	2.077	2.077	-2.714	-2
O	2.077	-2.077	-2.714	-2
Mg	-2.134	0.000	-2.729	2
Mg	-0.000	2.134	-2.729	2
Mg	2.134	0.000	-2.729	2
Mg	0.000	-2.134	-2.729	2

**Table S4.** Point charge crystal field for  $4f^{10}$  Dy<sup>br</sup> atoms. Coordinates (X,Y,Z) are provided in Å, while the charge intensity Q is given in multiples of electron charge.

Element	X	Y	Z	Q
O	-0.981	-0.981	-2.020	-2
O	0.981	0.981	-2.020	-2
Mg	-1.115	1.115	-2.503	2
Mg	1.115	-1.115	-2.503	2

Corresponding simulated XAS and XMCD spectra of the 4 species are shown in Fig. S2. For all species, the normal and grazing incidence spectra are calculated with the magnetic field and photon beam parallel to and at 60 degrees from the surface normal, respectively. For the bridge species, the magnetic field and photon axis in grazing incidence are oriented at an azimuth angle of 45 degrees with respect to the O-Dy-O bond. Except for the  $4f^9 \text{ Dy}^{\text{br}}$ , all species show pronounced angular dependence of the XAS and perpendicular magnetic anisotropy. Conversely,  $4f^9 \text{ Dy}^{\text{br}}$  show a strong in-plane anisotropy. The presence of two  $4f^9$  species with opposite anisotropy results in a negligible XMCD angular dependence for  $t_{\text{MgO}} < 4 \text{ ML}$  since, for these thicknesses, the signal is largely dominated by the two  $4f^9$  species, as discussed in the main text.

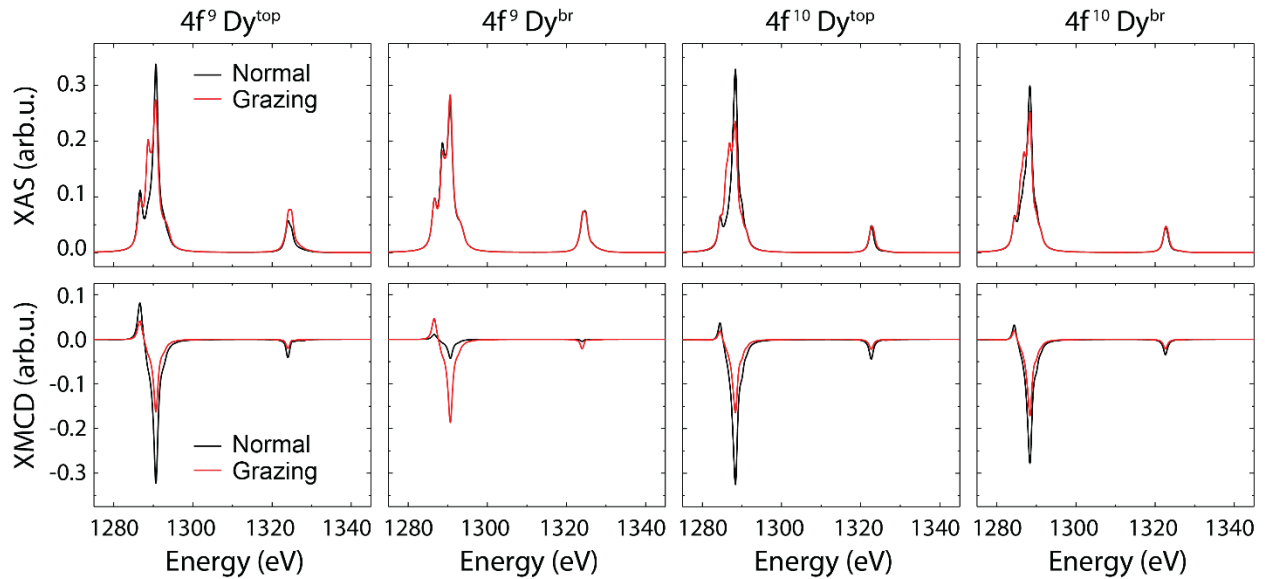


**Figure S2.** Simulated spectra for the four Dy species calculated for normal (black lines) and grazing incidence (red lines) for an applied field  $B = 6.8 \text{ T}$  and a temperature  $T = 2.5 \text{ K}$ .

#### 4. Fit of the XAS spectra

The simulated XAS of the 4 species shown in Fig. S2 have been used to identify the composition of the ensemble. As also pointed out for the case of Ho atoms on MgO,<sup>8,9</sup> the very long magnetic lifetime of  $4f^9$  Dy<sup>top</sup> at large fields does not allow the ensemble to attain magnetic saturation, resulting in reduced intensity of XMCD. Due to this effect, it is not possible to perform a correct fit of the XMCD using simulated spectra from multiplet calculations. On the other hand, XAS spectra are essentially insensitive to the magnetization of the ensemble, allowing meaningful comparison with simulations. The use of only XAS spectra in the fitting procedure allows us to reliably distinguish species with different 4f occupation due to the large difference in the spectral shape between  $4f^9$  and  $4f^{10}$ , see Fig S2. On the other hand, the precision of the individual adsorption site abundance is expected to be low as the differences between XAS spectra of atoms with the same 4f occupation are not very pronounced.

For every MgO thickness, simultaneous fit of the normal and grazing incidence XAS was used to identify the amount of  $4f^9$  vs.  $4f^{10}$  species. Results of the individual fitting are shown in Fig. S3. The relative abundance of the Dy  $4f^9$  and  $4f^{10}$  species as a function of the MgO thickness are summarized in Table S5. Summed values for each 4f occupation from the same table are plotted in Fig. 1c of the main text.

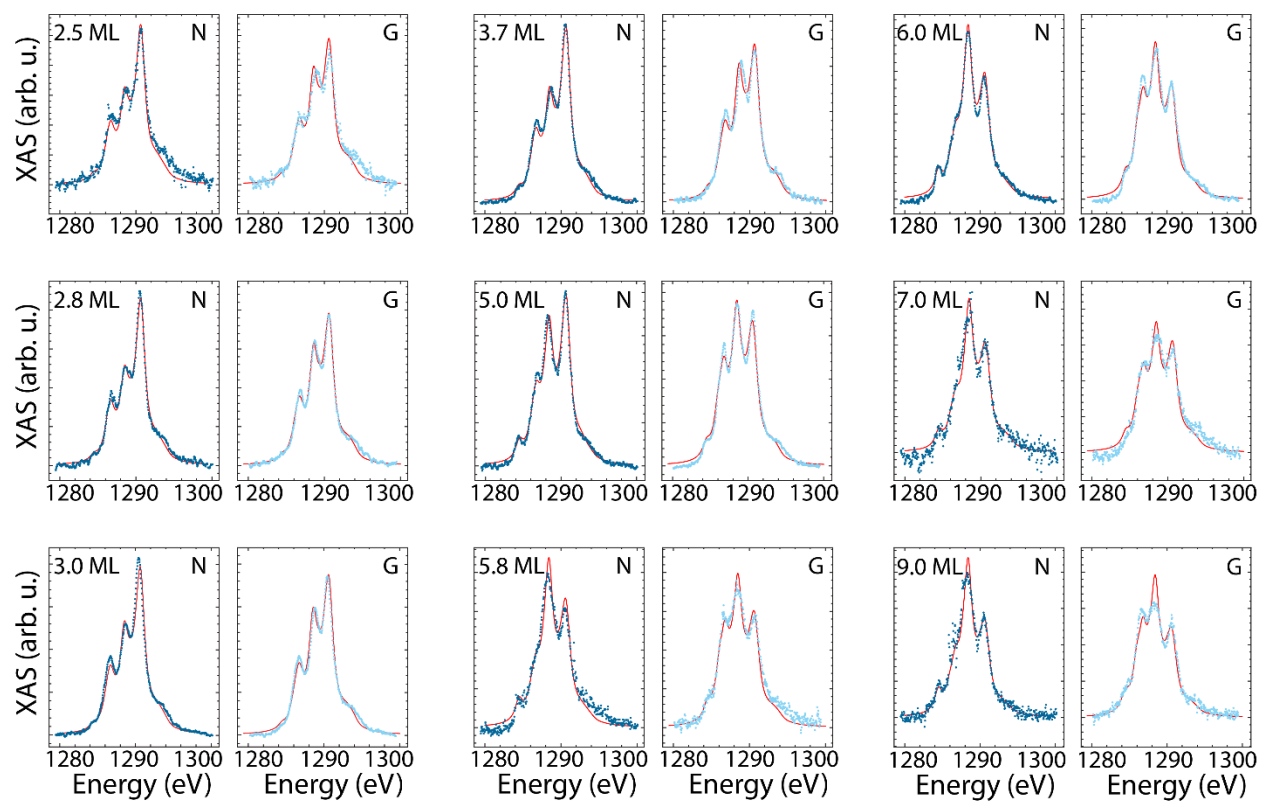


**Figure S3.** Individual fit of the experimental XAS performed using simulated spectra from multiplets. For every spectrum, the panels show the corresponding MgO thickness in ML and the sample orientation with respect to the field (N normal incidence, G grazing incidence).

**Table S5.** Abundance of Dy species considered in the fit using calculated spectra from multiplet calculations. Shown are also the summed abundance of  $4f^9$  and  $4f^{10}$  occupations plotted in Fig. 1c of the main text.

$t_{\text{MgO}}$ (ML)	$4f^9 \text{ Dy}^{\text{top}}$	$4f^9 \text{ Dy}^{\text{br}}$	$4f^{10} \text{ Dy}^{\text{top}}$	$4f^{10} \text{ Dy}^{\text{br}}$	Sum $4f^9$	Sum $4f^{10}$
<b>2.5</b>	$45 \pm 3 \%$	$39 \pm 3 \%$	$7 \pm 6 \%$	$9 \pm 7 \%$	$84 \pm 4 \%$	$16 \pm 4 \%$
<b>2.8</b>	$47 \pm 1 \%$	$38 \pm 1 \%$	$10 \pm 2 \%$	$5 \pm 3 \%$	$84 \pm 2 \%$	$16 \pm 2 \%$
<b>3.0</b>	$32 \pm 2 \%$	$52 \pm 2 \%$	$0 \pm 3 \%$	$16 \pm 4 \%$	$84 \pm 2 \%$	$16 \pm 2 \%$
<b>3.7</b>	$48 \pm 1 \%$	$29 \pm 2 \%$	$12 \pm 3 \%$	$11 \pm 3 \%$	$77 \pm 2 \%$	$23 \pm 2 \%$
<b>5.0</b>	$52 \pm 1 \%$	$6 \pm 1 \%$	$33 \pm 2 \%$	$9 \pm 3 \%$	$58 \pm 2 \%$	$42 \pm 2 \%$
<b>5.8</b>	$27 \pm 3 \%$	$20 \pm 3 \%$	$43 \pm 6 \%$	$45 \pm 7 \%$	$47 \pm 4 \%$	$53 \pm 4 \%$
<b>6.0</b>	$27 \pm 1 \%$	$18 \pm 1 \%$	$44 \pm 3 \%$	$11 \pm 3 \%$	$45 \pm 2 \%$	$55 \pm 2 \%$
<b>7.0</b>	$6 \pm 3 \%$	$47 \pm 3 \%$	$27 \pm 6 \%$	$20 \pm 7 \%$	$53 \pm 4 \%$	$47 \pm 4 \%$
<b>9.0</b>	$21 \pm 2 \%$	$17 \pm 2 \%$	$31 \pm 5 \%$	$31 \pm 6 \%$	$38 \pm 3 \%$	$62 \pm 3 \%$

## 5. Anisotropy of the hysteresis loops

As discussed in the main text, XMCD spectra of ensembles with large majority of  $4f^9$  species show very little angular dependence. In line with this finding, hysteresis loops acquired at the  $4f^9$  peak of the XMCD spectra also show negligible angular dependence, with minor narrowing of the hysteresis area in grazing incidence, see Fig. S4. As discussed, we attribute this lack of angular dependence to the dominant contribution of the two  $4f^9$  species with opposite anisotropy.

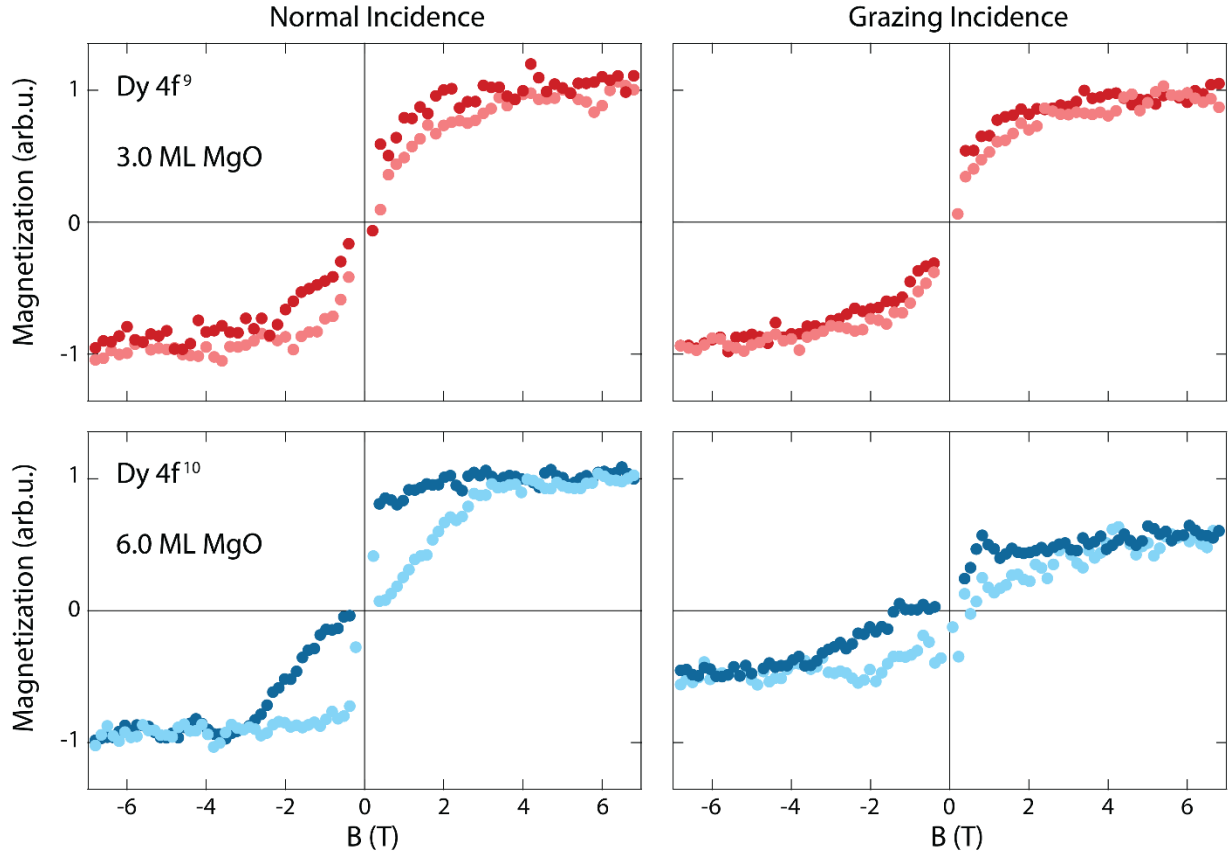


**Figure S4.** Angular dependent hysteresis loops acquired at the  $4f^9$  (top panels) and  $4f^{10}$  peaks (bottom panels) for two different samples.

Conversely, ensembles with majority of  $4f^{10}$  species show stronger XMCD signal at normal incidence. Accordingly, the spectra acquired at the corresponding peak show larger magnetization along the normal incidence. We attribute this behavior to the fact that both  $4f^{10}$  species show perpendicular anisotropy, see Fig. S2.

## 6. Details of DFT calculations

To investigate the adsorption geometry and electronic configuration of Dy on thin layers of MgO, we performed density functional theory (DFT) calculations using pseudopotentials and plane wave bases as implemented in Quantum Espresso.<sup>10, 11</sup> The system setup consists of 4 monolayers (ML) of silver exposing the (100) surface expanded into a 3x3 lateral supercell capped by 2 ML of MgO and 15 Å of vacuum. Dy is placed on top of either oxygen or a bridge site and the system was relaxed until the residual forces were less than  $10^{-3}$  Ry/ $a_0$  ( $a_0$  is the Bohr radius). Highly localized electronic manifolds such as the f-shell and d-shell are prone to systematic errors due to self-interaction of the exchange-correlation functional leading to fractional electron occupations. To correct for this we applied a Hubbard U correction of 9 eV on the 4f and 5d manifolds, which drastically improves the occupations of the respective shells.<sup>12, 13</sup> Pseudopotentials were chosen according to the SSSP efficiency table except for the silver pseudopotential which was taken from the PSL library (version 0.3.1) expanded into plane waves using a kinetic cutoff of 40 Ry and a cutoff for the charge density of 400 Ry.<sup>14, 15</sup> All pseudopotentials use the projector augmented wave (PAW) method and the Perdew-Burker-Enzerhofer (PBE) parametrization for the exchange-correlation potential.<sup>16, 17</sup> The Brillouin zone was sampled using a 3x3x1 Monkhorst-Pack grid and we apply a smearing of about 160 K for the electronic states. We find that the magnetic states of the Dy are not affected by the k-point sampling beyond the chosen grid nor the electronic broadening between 16 and 1000 K as they are basically non-dispersive.

For the case of MgO/Ag(100), we find, in good approximation, a singly charged Dy for both adsorption sites with 4f occupancy close to  $4f^9$ . We note that the substrate plays an important role

in lowering the energy of the 6s states relative to the 4f states, as a singly charged Dy in vacuum would adopt a  $6s^1 4f^{10}$  configuration based on our calculations. The results are summarized in Table S5. Also shown in Table S6 is the spin polarization (the difference between up and down Löwdin charges), which is almost completely due to the 4f electrons, while only negligible amount is localized on the valence 5d6s orbitals.

**Table S6.** Calculated electronic configuration of Dy atoms on MgO and MgO/Ag(100). The polarization is calculated as the difference between majority and minority Löwdin charges ( $n_{\text{up}} - n_{\text{down}}$ ) for the indicated orbitals. The free-atom configuration is provided as reference.

Site	Substrate	Dy charge	Configuration	Polarization
-	Free atom	+0.0 e	$4f^{10.0} 6s^{2.0} 5d^{0.0}$	$4f^{5.0} 6s^{0.0} 5d^{0.0}$
Top	MgO/Ag(100)	+0.7 e	$4f^{9.3} 6s^{1.5} 5d^{0.4}$	$4f^{4.7} 6s^{0.0} 5d^{0.0}$
Top	MgO	+0.4 e	$4f^{10} 6s^{1.5} 5d^{0.2}$	$4f^{3.9} 6s^{0.0} 5d^{0.0}$
Bridge	MgO/Ag(100)	+0.6 e	$4f^{9.1} 6s^{1.3} 5d^{1.1}$	$4f^{4.9} 6s^{0.3} 5d^{0.2}$
Bridge	MgO	+0.4 e	$4f^{10.0} 6s^{1.2} 5d^{0.2}$	$4f^{4.0} 6s^{0.0} 5d^{0.0}$

To study the co-existence of different charge states we remove the silver and thereby the ability of the Dy to give a charge to the metal support substrate. We then remove one electron from the entire system which we denote as  $[\text{MgO}]^{+1}$ , which in excellent agreement reproduces the electronic configuration of Dy on MgO/Ag(100). By restoring the neutral cell ( $[\text{MgO}]^{+0}$ ) we find a close to  $6s^2 4f^{10}$  electronic configuration, indicating that a neutral species exists when the charge transfer to the metal substrate is suppressed by sufficiently thick MgO layers. The resulting density of states (DOS) projected onto atomic states is shown for each system in Fig. S5. Additional calculations



for the bridge absorption site (see Table S6 and Fig. S6) give similar results indicating that for thin layers of MgO a close to  $6s^2 4f^9$  electronic configuration corresponding to a formal  $Dy^{+1}$  is adopted.

Consecutive relaxations of the system after removing the Ag layer have not shown any instabilities of these very thin layers. We further confirm the stability of the free-standing MgO layer by comparison with calculated Dy on 4 ML MgO. The change in geometry when increasing the MgO layer thickness is less than 0.02 Å for the  $Dy^{top}$ , indicating very minor differences with respect to the free-standing 2 ML MgO substrate, see Table S7.

**Table S7.** Calculated charge state and atomic distances between Dy and underneath O ( $d_{Dy-O}$ ), neighboring Mg ( $d_{Dy-Mg}$ ), and relative height with respect to the MgO surface for different substrates.

	Charge state	$d_{Dy-O}$ (Å)	$d_{Dy-Mg}$ (Å)	$h_{Dy}$ (Å)
<b>2 ML MgO/Ag(100)</b>	+0.6 e	2.1015	3.5031	2.821
<b>2 ML MgO</b>	+0.4 e	2.2041	3.4640	2.762
<b>4 ML MgO</b>	+0.4 e	2.225	3.452	2.737

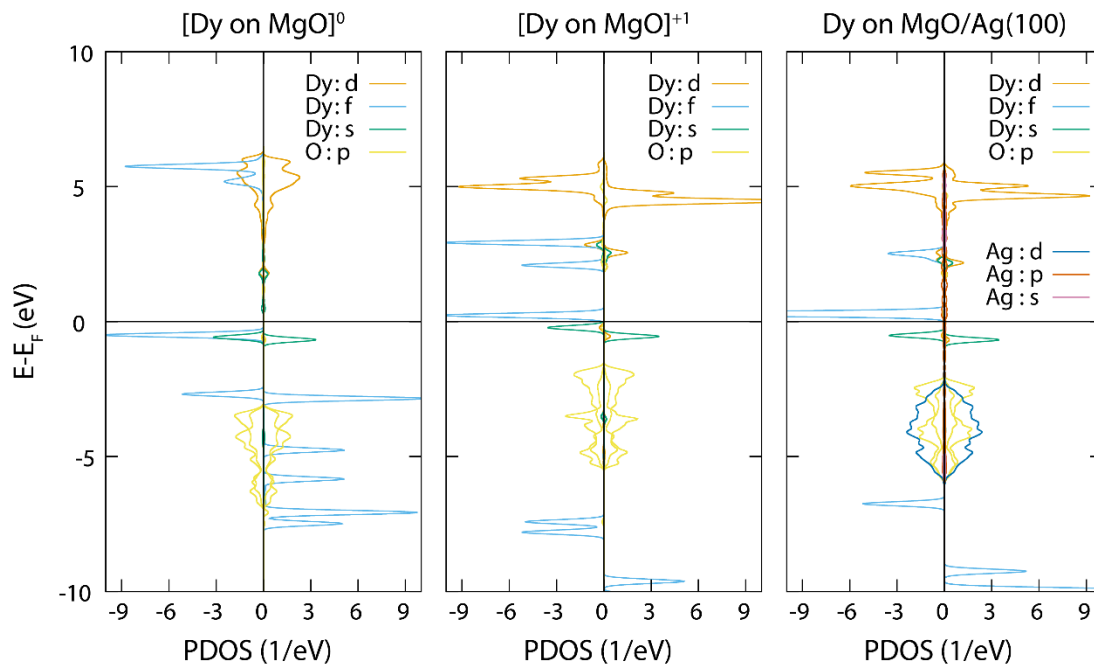


**Figure S5.** PDOS of  $\text{Dy}^{\text{top}}$  calculated for adsorption on O-top site of MgO for neutral and charged slab, as well as for MgO/Ag(100).

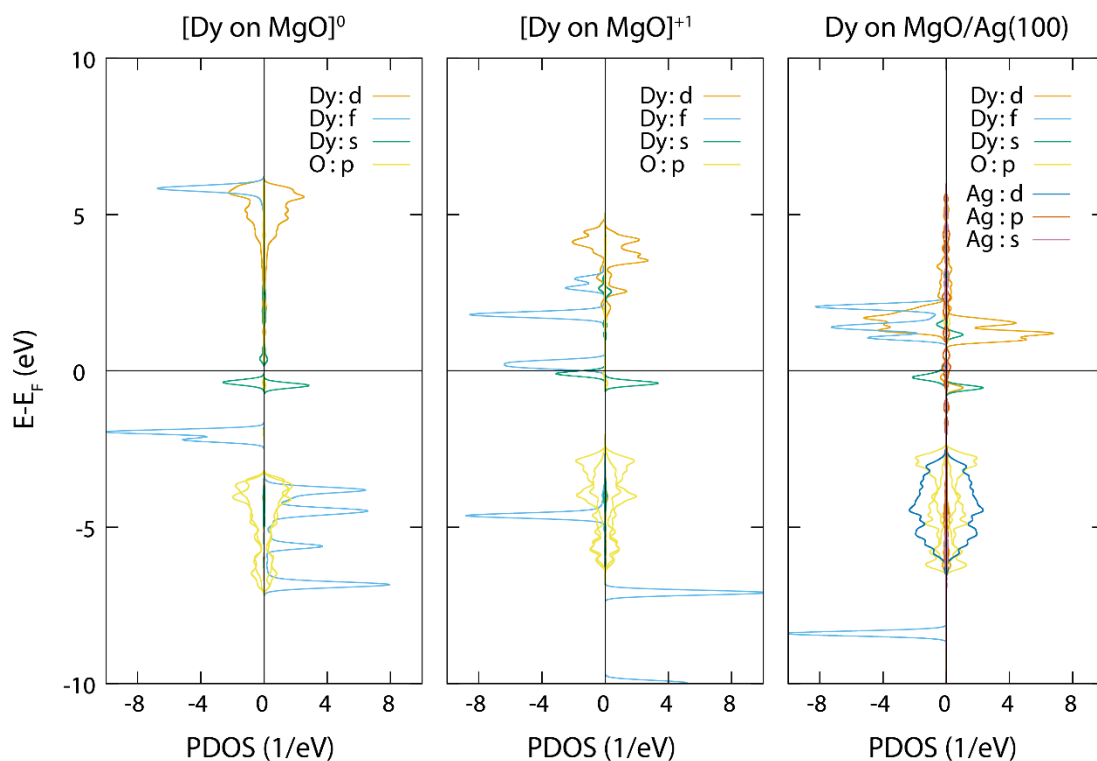


**Figure S6.** PDOS of Dy<sup>br</sup> calculated for adsorption on bridge site of MgO for neutral and charged slab, as well as for MgO/Ag(100).

## 7. Quantum levels of Dy at the bridge site

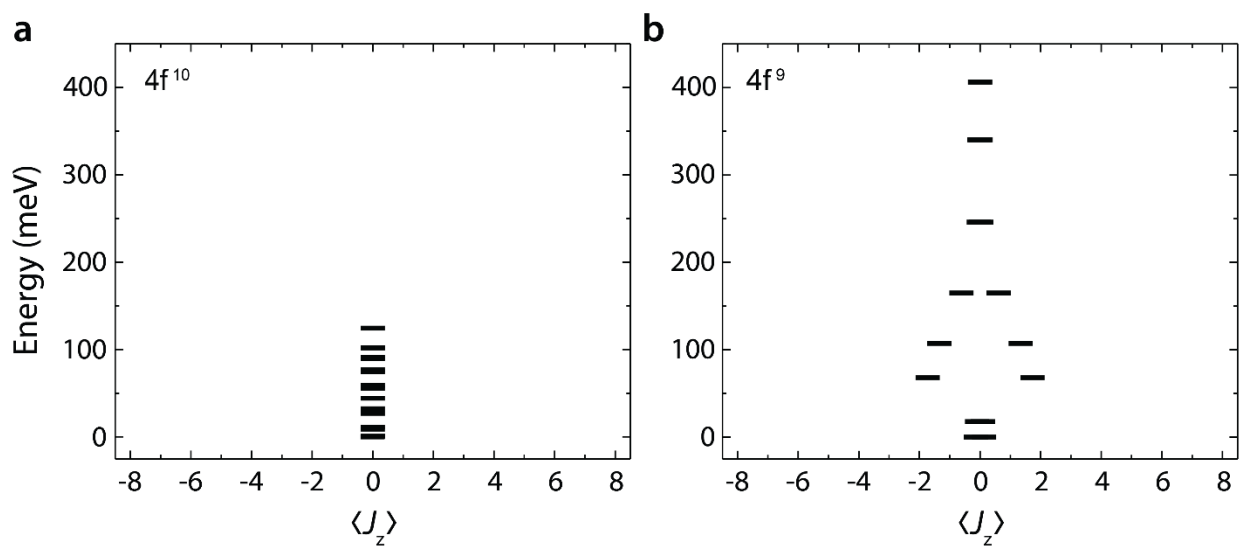


**Figure S7.** (a) Quantum levels of 4f<sup>10</sup> Dy<sup>br</sup> and 4f<sup>9</sup> Dy<sup>br</sup> obtained from multiplet calculations.

## 8. Model for electrostatic energy at the oxide layer

For lanthanide atoms, the occupation of 4f orbitals is generally dictated by the balance between atomic energy to promote one electron from the 4f to the outer shells and the energy gain in bonding formation/charge transfer to the substrate.<sup>18</sup> In the case of Dy atoms on MgO/Ag(100), the energy gain related to the charge transfer to the substrate and the stronger bond formation overcomes the configurational energy penalty required for the atoms to change from the neutral atomic 4f<sup>10</sup> to the bulk-like 4f<sup>9</sup> configuration. Hence, the configuration with singly ionized 4f<sup>9</sup> species is attained, as shown by our DFT calculations. However, the thickness of the oxide layer provides another source of electrostatic energy cost that increases with the thickness of the dielectric. Above a critical thickness, the electrostatic energy becomes too large and makes both the charge transfer to the substrate and related 4f<sup>9</sup> configuration unfavorable. Using a simple plane capacitor model, we estimate the additional electrostatic energy induced by the charged 4f<sup>9</sup> atoms at the surface of the MgO film as  $E = \frac{1}{2C} q^2$ , with  $C$  being the capacity of the dielectric film and  $q$  the total charge at the surface. Using quantities defined per unit of area ( $A$ ), such as  $c = \frac{C}{A} = \epsilon_0 \epsilon_r / (t_{MgO} a_{MgO})$  and  $\sigma = \frac{q}{A} = e n_{Dy}$ , we obtain a surface energy density  $\varepsilon = \frac{E}{A} = \frac{e^2 a_{MgO}}{2\epsilon_0 \epsilon_r} t_{MgO} n_{Dy}^2$ . Taking tabulated values for the MgO lattice constant  $a_{MgO} = 212$  pm, relative permittivity  $\epsilon_r = 9.9$ , and a surface coverage of 0.01 ML of Dy corresponding to a density  $n_{Dy} = 1.11 \times 10^{17}$  atoms/m<sup>2</sup>, we find the specific electrostatic energy  $\frac{\varepsilon}{(t_{MgO} n_{Dy})} = 21.5$  meV per MgO layer per Dy atom. By estimating the crossover between the two configurations to occur at around 7 layers, the required electrostatic energy to overcome the configurational difference between 4f<sup>9</sup> and 4f<sup>10</sup> amounts to about 150 meV per Dy atom. Although this simple model neglects other MgO thickness-related effects, such as the variation of the work function,<sup>19</sup> the obtained value for the

configurational crossover is of the same order of magnitude of that estimated for Dy divalent compounds.<sup>20</sup>

## SUPPLEMENTARY REFERENCES

1. Donati, F.; Rusponi, S.; Stepanow, S.; Wäckerlin, C.; Singha, A.; Persichetti, L.; Baltic, R.; Diller, K.; Patthey, F.; Fernandes, E.; Dreiser, J.; Šljivančanin, Z.; Kummer, K.; Nistor, C.; Gambardella, P.; Brune, H., Magnetic remanence in single atoms. *Science* **2016**, *352* (6283), 318-21.
2. Fernandes, E.; Donati, F.; Patthey, F.; Stavrić, S.; Šljivančanin, Ž.; Brune, H., Adsorption sites of individual metal atoms on ultrathin MgO(100) films. *Phys. Rev. B* **2017**, *96* (4), 045419.
3. Fernandes, E. Adsorption Sites of Metal Atoms on MgO Thin Films and Rotational Quantum State Spectroscopy of Physisorbed H<sub>2</sub>. Ph.D. thesis; EPFL, Lausanne, 2017.
4. Piamonteze, C.; Flechsig, U.; Rusponi, S.; Dreiser, J.; Heidler, J.; Schmidt, M.; Wetter, R.; Calvi, M.; Schmidt, T.; Pruchova, H.; Krempasky, J.; Quitmann, C.; Brune, H.; Nolting, F., X-Treme beamline at SLS: X-ray magnetic circular and linear dichroism at high field and low temperature. *J. Synchrotron Radiat.* **2012**, *19* (Pt 5), 661-74.
5. Dreiser, J.; Westerström, R.; Piamonteze, C.; Nolting, F.; Rusponi, S.; Brune, H.; Yang, S.; Popov, A.; Dunsch, L.; Greber, T., X-ray induced demagnetization of single-molecule magnets. *Applied Physics Letters* **2014**, *105* (3), 032411.
6. Uldry, A.; Vernay, F.; Delley, B., Systematic computation of crystal-field multiplets for x-ray core spectroscopies. *Phys. Rev. B* **2012**, *85* (12), 125133.
7. Singha, A.; Willke, P.; Bilgeri, T.; Zhang, X.; Brune, H.; Donati, F.; Heinrich, A. J.; Choi, T., Engineering atomic-scale magnetic fields by dysprosium single atom magnets. *Nat. Commun.* **2021**, *12* (1), 4179.
8. Natterer, F. D.; Donati, F.; Patthey, F.; Brune, H., Thermal and Magnetic-Field Stability of Holmium Single-Atom Magnets. *Phys. Rev. Lett.* **2018**, *121* (2), 027201.
9. Donati, F., Magnetic Relaxation Mechanisms in Ho Single Atom Magnets. *J. Magn.* **2020**, *25* (4), 441-452.
10. Giannozzi, P.; Baroni, S.; Bonini, N.; Calandra, M.; Car, R.; Cavazzoni, C.; Ceresoli, D.; Chiarotti, G. L.; Cococcioni, M.; Dabo, I.; Dal Corso, A.; de Gironcoli, S.; Fabris, S.; Fratesi, G.; Gebauer, R.; Gerstmann, U.; Gougoussis, C.; Kokalj, A.; Lazzeri, M.; Martin-Samos, L.; Marzari, N.; Mauri, F.; Mazzarello, R.; Paolini, S.; Pasquarello, A.; Paulatto, L.; Sbraccia, C.; Scandolo, S.; Sclauzero, G.; Seitsonen, A. P.; Smogunov, A.; Umari, P.; Wentzcovitch, R. M., QUANTUM ESPRESSO: a modular and open-source software project for quantum simulations of materials. *J. Phys.: Condens. Matter* **2009**, *21* (39), 395502.
11. Giannozzi, P.; Andreussi, O.; Brumme, T.; Bunau, O.; Buongiorno Nardelli, M.; Calandra, M.; Car, R.; Cavazzoni, C.; Ceresoli, D.; Cococcioni, M.; Colonna, N.; Carnimeo, I.; Dal Corso, A.; de Gironcoli, S.; Delugas, P.; DiStasio, R. A.; Ferretti, A.; Floris, A.; Fratesi, G.; Fugallo, G.; Gebauer, R.; Gerstmann, U.; Giustino, F.; Gorni, T.; Jia, J.; Kawamura, M.; Ko, H. Y.; Kokalj, A.; Küçükbenli, E.; Lazzeri, M.; Marsili, M.; Marzari, N.; Mauri, F.; Nguyen, N. L.; Nguyen, H. V.; Otero-de-la-Roza, A.; Paulatto, L.; Poncé, S.; Rocca, D.; Sabatini, R.; Santra, B.; Schlipf, M.; Seitsonen, A. P.; Smogunov, A.; Timrov, I.;

- Thonhauser, T.; Umari, P.; Vast, N.; Wu, X.; Baroni, S., Advanced capabilities for materials modelling with Quantum ESPRESSO. *J. Phys.: Condens. Matter* **2017**, *29* (46), 465901.
12. Dal Corso, A., Pseudopotentials periodic table: From H to Pu. *Comput. Mater. Sci.* **2014**, *95*, 337-350.
  13. Prandini, G.; Marrazzo, A.; Castelli, I. E.; Mounet, N.; Marzari, N., Precision and efficiency in solid-state pseudopotential calculations. *Npj Comput. Mater.* **2018**, *4* (1), 72.
  14. Blöchl, P. E., Projector augmented-wave method. *Phys. Rev. B* **1994**, *50* (24), 17953-17979.
  15. Perdew, J. P.; Burke, K.; Ernzerhof, M., Generalized Gradient Approximation Made Simple. *Phys. Rev. Lett.* **1996**, *77* (18), 3865-3868.
  16. Leiria Campo Jr, V.; Cococcioni, M., Extended DFT +U+V method with on-site and inter-site electronic interactions. *J. Phys.: Condens. Matter* **2010**, *22* (5), 055602.
  17. Topsakal, M.; Wentzcovitch, R. M., Accurate projected augmented wave (PAW) datasets for rare-earth elements (RE = La-Lu). *Comput. Mater. Sci.* **2014**, *95*, 263-270.
  18. Singha, A.; Baltic, R.; Donati, F.; Wäckerlin, C.; Dreiser, J.; Persichetti, L.; Stepanow, S.; Gambardella, P.; Rusponi, S.; Brune, H., 4f-occupancy and magnetism of rare-earth atoms adsorbed on metal substrates. *Phys. Rev. B* **2017**, *96* (22), 224418.
  19. Hurdax, P.; Hollerer, M.; Puschnig, P.; Lüftner, D.; Egger, L.; Ramsey, M. G.; Sterrer, M., Controlling the Charge Transfer across Thin Dielectric Interlayers. *Adv. Mater. Interfaces* **2020**, *7* (14), 2000592.
  20. Fieser, M. E.; MacDonald, M. R.; Krull, B. T.; Bates, J. E.; Ziller, J. W.; Furche, F.; Evans, W. J., Structural, Spectroscopic, and Theoretical Comparison of Traditional vs Recently Discovered Ln<sup>2+</sup> Ions in the [K(2.2.2-cryptand)][(C<sub>5</sub>H<sub>4</sub>SiMe<sub>3</sub>)<sub>3</sub>Ln] Complexes: The Variable Nature of Dy<sup>2+</sup> and Nd<sup>2+</sup>. *J. Am. Chem. Soc.* **2015**, *137* (1), 369-382.